Rapid interfacial exchange of Li ions dictates high Coulombic efficiency in Li metal anodes

Richard May,[a] Keith J. Fritzsching,[b] Dimitri Livitz,[a] Steven R. Denny,[a] and Lauren E. Marbella[a]*

[a]Department of Chemical Engineering, Columbia University, New York, New York 10027

[b]Department of Chemistry, Columbia University, New York, New York 10027

AUTHOR INFORMATION

Corresponding Author

*Lauren E. Marbella – Fu Foundation School of Engineering and Applied Science, Department of Chemical Engineering, Columbia University, New York, New York 10027, United States; https://orcid.org/0000-0003-1639-3913; Email: lem2221@columbia.edu

ABSTRACT. Although Li metal batteries offer the highest possible specific energy density, practical application is plagued by Li filament growth with adverse effects on both Coulombic efficiency and battery safety. The structure and resulting properties of the solid electrolyte interphase (SEI) on Li metal is critical to controlling Li deposition morphologies and achieving high efficiency batteries. In this report, we use a combination of nuclear magnetic resonance (NMR) spectroscopy and X-ray photoelectron spectroscopy (XPS) to show that fast Li transport and low solubility at the electrode/SEI interface in 0.5 M $LiNO_3$ + 0.5 M LiTFSI electrolyte bi-salt in 1,3-dioxolane:dimethoxyethane (DOL:DME, 1:1, v/v) are responsible for the formation of

low surface area Li deposits and high Coulombic efficiency, despite the fact that the SEI is thicker and chemically more heterogeneous than LiTFSI alone. These data suggest that SEI design strategies that increase SEI stability and Li interfacial exchange rate will lead to more even current distribution, ultimately providing a new framework to generate smooth Li morphologies during plating/stripping.

TOC GRAPHICS

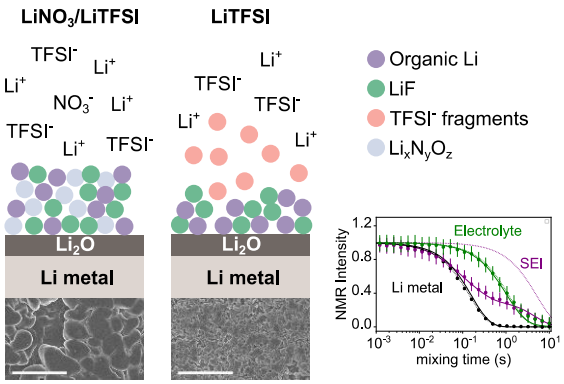

Leveraging the exceptionally high specific capacity of Li metal anodes is critical to realizing many emerging next generation battery technologies such as Li-S,[1,2] Li-air,[3–6] and all solid-state batteries.[7–11] However, challenges surrounding the reversibility of Li deposition have severely limited the cycling efficiency of Li metal batteries.[12–22] Immediately upon contact with liquid electrolytes, Li metal anodes develop a solid electrolyte interphase (SEI) that is comprised of electrolyte decomposition products.[23,24] Instabilities in the SEI on rechargeable Li metal anodes create local heterogeneities in current distribution during Li stripping/plating.[12,16,25–29] The

resulting uneven Li deposition architectures (i.e., Li filaments) lead to low Coulombic efficiency (CE) and eventually, cell failure.[13,30–40] Li filament growth can also contact the cathode, leading to short-circuiting events and serious safety hazards.[12,17,20,21,41–44]

It is well-established that electrolyte formulation can be leveraged to tune Li deposition morphologies,[13,15,24,45,46] likely by altering SEI composition and arrangement. Claims that a thinner, more homogeneous SEI is correlated with smooth Li deposition and high CE are ubiquitous in the literature,[13,15,47–58] likely due to the fact that uncontrolled SEI growth can hinder Li transport to the underlying electrode. However, recent reports indicate that the SEI formed in high performance LiTFSI/$LiNO_3$ salt mixtures in ether-based solvents is actually thicker than the SEI on Li metal compared to LiTFSI alone.[30,59] The presence of the salt additive ($LiNO_3$) also deposits additional $Li_xN_yO_z$ reduction products on the surface of Li metal, increasing the compositional complexity of the SEI.[2,60–63] Taken together, these findings strongly suggest that we must carefully reevaluate the assumed relationship between SEI thickness/heterogeneity and CE/deposition morphology in Li metal batteries.

Here, we use a combination of scanning electron microscopy (SEM), electrochemical measurements, nuclear magnetic resonance (NMR) spectroscopy, and X-ray photoelectron spectroscopy (XPS) to identify the molecular origin of performance enhancement of upon addition of $LiNO_3$ to Li metal anodes cycled in 1,3-dioxalane:dimethoxyethane (DOL:DME, 1:1, v/v). Comparison of the electrochemical performance and Li deposition morphologies for 1 M LiTFSI, 0.5 M LiTFSI, and 0.5 M $LiNO_3$ + 0.5 M LiTFSI show substantially higher CE values and low surface area Li deposits in the presence of $LiNO_3$. Remarkably, quantitative NMR and XPS demonstrate that the SEI formed in electrolytes containing $LiNO_3$ are thicker and more heterogeneous (i.e., contain more diverse chemical compounds), suggesting that these parameters

do not dictate plating morphologies. Detailed analysis of spin-lattice (T_1) relaxation and exchange spectroscopy (EXSY) NMR measurements show that enhanced electrochemical performance for $LiNO_3$-containing bisalts is instead correlated with an increased Li exchange rate between Li metal and the SEI. Higher Li exchange rates are concomitant with $Li_xN_yO_z$ decomposition products in the SEI and decreased SEI solubility, suggesting that improving interfacial conductivity and stability are key to SEI engineering efforts.

Li deposition behavior in ether solvent with and without $LiNO_3$ was examined via post mortem SEM analysis. Both 1 M LiTFSI and 0.5 M LiTFSI in DOL:DME (1:1 v/v) result in the formation of high surface area Li deposits (Figure 1a, b) and poor CEs (74% for 0.5 LiTFSI and 86% for 1 M LiTFSI after five cycles, followed by a rapid decline to approximately 45% over 100 cycles, Figure 1d). Upon addition of $LiNO_3$ to the electrolyte (0.5 M $LiNO_3$ + 0.5 M LiTFSI in DOL:DME), the Li deposits observed after galvanostatic polarization exhibit flat, bud-like

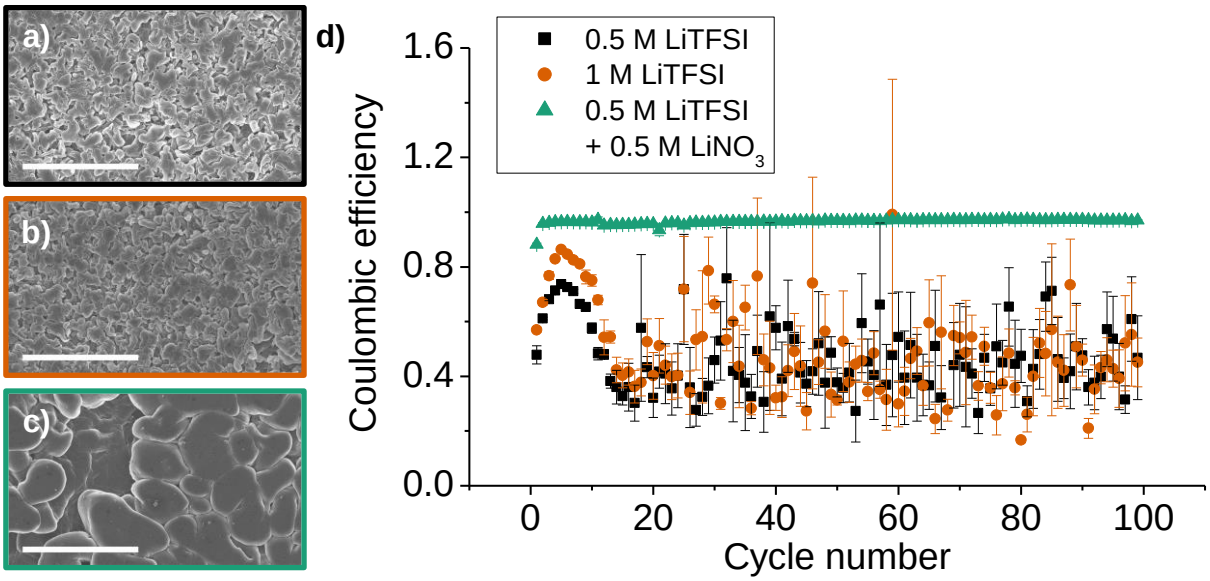

Figure 1. SEM data showing Li microstructural morphology in a) 0.5 M LiTFSI and b) 0.5 M LiTFSI + 0.5 M $LiNO_3$ after galvanostatic polarization at 1 mA cm^{-2} for 2 h in Li/Li symmetrical coin cells. Scale bar = 30 μm. c) CE measurements for 0.5 M LiTFSI (black squares), 1 M LiTFSI (orange circles) and 0.5 M LiTFSI + 0.5 M $LiNO_3$ (green triangles) in Li/Cu half cells. Li was plated on Cu at 0.5 mA cm^{-2} for 1 h and stripped at 0.5 mA cm^{-2} to 1 V for each cycle. Error bars represent standard error for N = 3.

architectures (Figure 1c) and high CE (97%) over 100 cycles (Figure 1d). The observed trends in CE are consistent with increasing overpotentials for both 1 M and 0.5 M LiTFSI electrolytes and decreasing overpotential for 0.5 M $LiNO_3$ + 0.5 M LiTFSI electrolyte as a function of cycle number (Figure S1).

The high CE, smooth Li deposition behavior, and decreased overpotential upon addition of $LiNO_3$ suggests that $LiNO_3$ decomposition leads to changes in the SEI that are responsible for the improved battery performance. The impact of $LiNO_3$ addition on SEI composition was quantitatively evaluated with ^{7}Li MAS SSNMR measurements (Figure 2). ^{7}Li SSNMR shows two distinct resonances, one corresponding to the Li metal electrode (~265 ppm) and the other corresponding to Li in the SEI (~0 ppm). A combination of strong Li-Li dipole-dipole coupling and rapid Li ion exchange likely prevents resolution of discrete Li-containing compounds (e.g., Li_2O, LiF) in the SEI using single pulse NMR acquisition (Figure S9 shows that similar resolution

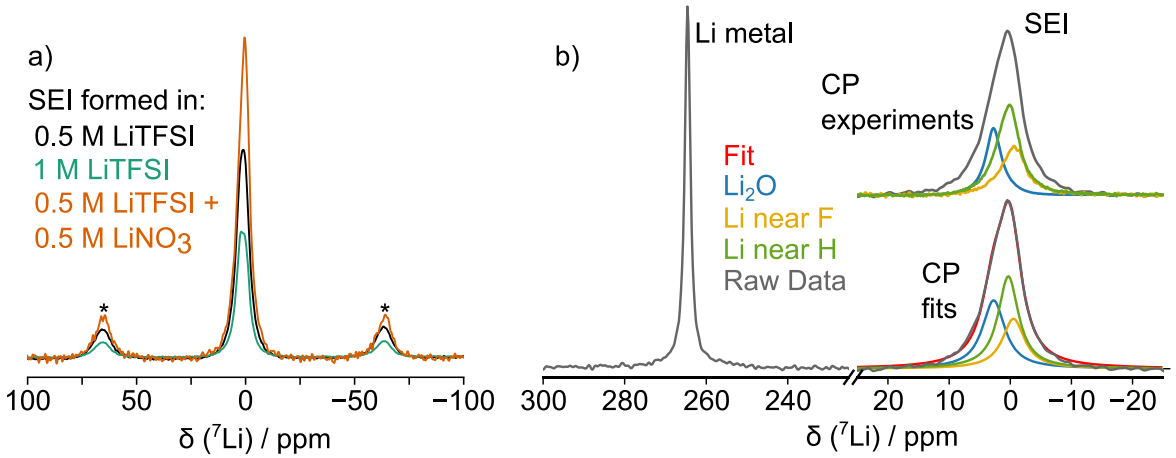

Figure 2. a) ^{7}Li SSNMR (MAS = 15 kHz) of electrolyte decomposition products cycled in 0.5 M LiTFSI (black), 1 M LiTFSI (green), and 0.5 M LiTFSI + 0.5 M $LiNO_3$ (orange). Li metal peak is cut out to highlight quantitative differences in the SEI peak at ~0 ppm, which correspond to the amount of Li-containing decomposition products and Li salt remaining on the Li electrode surface. b) ^{7}Li solid-state NMR spectrum (gray) along with SEI peak deconvolutions corresponding to Li_2O (blue), Li near F (yellow), Li near H (green), and the peak deconvolution sum (red) for a representative 0.5 M LiTFSI + 0.5 M $LiNO_3$ sample. Inset above the SEI peak show the weighted CP experiments along with the Li_2O (in a separate model compound sample) single pulse experiment used to deconvolute the full SEI peak in grey. Peak deconvolutions are fit using methods described in the experimental section. Asterisks denote spinning sidebands.

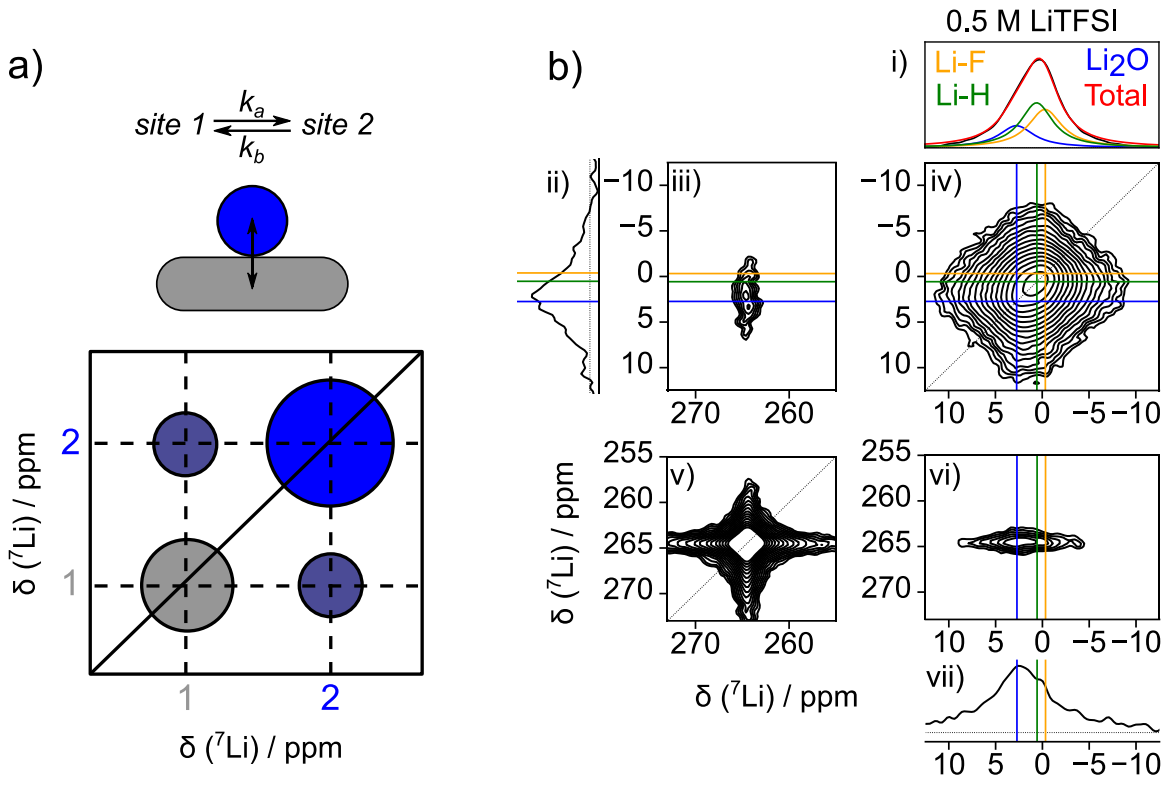

Figure 3. a) 2D ^{7}Li-^{7}Li EXSY cartoon showing chemical exchange between the SEI (red) and Li metal (blue) with cross peaks shown in purple. b) Representative 2D solid-state ^{7}Li-^{7}Li NMR EXSY contour plots and corresponding 1D slices for electrolyte decomposition products in 0.5 M LiTFSI. For each composition (a-b), the separate panels denote: i) 1D row slices at the LiF chemical shift in the indirect dimension (-0.33 ppm for 0.5 M LiTFSI and -0.52 ppm for LiTFSI/$LiNO_3$). ii) 1D column projections at the Li metal chemical shift in the direct dimension (264.5 ppm). iii-vi) Contour plots zoomed in to show SEI → metal exchange, SEI ↔ SEI exchange, metal ↔ metal exchange, and metal → SEI exchange respectively. vii) 1D row slices at the Li metal chemical shift in the indirect dimension. Data for1 M LiTFSI and 0.5 M LiTFSI + 0.5 M $LiNO_3$ are shown in Figure S20.

is obtained in ^{6}Li NMR, suggesting this is primarily due to Li exchange). ^{1}H→^{7}Li and ^{19}F→^{7}Li cross polarization magic-angle spinning (CPMAS) solid-state NMR (SSNMR) were used to transfer magnetization between individual nuclei and resolve the chemical shift and full width at half maximum (fwhm) values that correspond to individual compounds in the SEI. In the cross-polarization (CP) experiment, magnetization transfer from nucleus A (e.g., ^{1}H) to a separate nucleus B (e.g., ^{7}Li) results in NMR signal from B nuclei which are close in space (< 3 nm) to A nuclei. From ^{1}H→^{7}Li and ^{19}F→^{7}Li CPMAS, Li species near ^{1}H (i.e., organic compounds, such as PEO, Figure 2b, green) and Li species near ^{19}F (i.e., LiTFSI/LiF, Figure 2b, yellow) can be clearly

assigned. After fitting the CP spectra (Figures S10-12; a, b), the high frequency portion of the Li-containing SEI is still unaccounted for. The remaining peak volume is attributed to Li from the native Li_2O layer on Li metal, as this region corresponds well to the ^7Li shift for pure Li_2O at 2.9 ppm (Figure 2, blue spectrum). (N.B. the fwhm of the Li_2O resonance is broadened during fitting, likely due to electron-nuclear coupling from direct bonding between Li metal and Li_2O at the metal/SEI interface, vide infra, Figure 3b).

Quantitative analysis of the ^7Li MAS SSNMR spectra for different electrolyte formulations indicates that the Li-containing SEI in the $LiNO_3$ electrolyte is 45% thicker than in the 0.5 M LiTFSI electrolyte and 140% thicker than in the 1 M LiTFSI electrolyte. Increased SEI thickness in the presence of $LiNO_3$ is also supported by ^{19}F and ^{13}C SSNMR (Figures S6, S7). When cycled in $LiNO_3$/LiTFSI, the SEI on Li metal exhibits ~40% more LiF than in pure LiTFSI electrolytes and 100% more PEO than in 0.5 M LiTFSI (PEO was not detected in the 1 M LiTFSI sample). We see that the Li-containing SEI in pure LiTFSI electrolytes is dominated by Li_2O (Figures S10d, S11d), while $LiNO_3$-containing electrolytes have a more heterogeneous distribution of Li environments (Figure S12d) with large quantities of Li near H (consistent with the relatively high amounts of PEO observed using ^{13}C SSNMR, Figure S7).

Having eliminated SEI thickness and homogeneity as factors that reliably correlate with battery performance, we next use EXSY[64] to examine Li transport at the metal/SEI interface. All EXSY experiments are performed *ex situ* and thus, measure Li transport under equilibrium conditions. These equilibrium conditions mean that during the course of the EXSY experiment, the sample itself does not change, but slow (on the NMR timescale) chemical exchange between magnetically inequivalent (i.e., spectrally resolved) sites are measured.[65] This approach has been successfully used to monitor ion hopping between distinct crystallographic sites in Li ion

conductors (which allows mapping of diffusion pathways),[66–74] exchange across grain boundaries in solid electrolytes,[75–78] and transport across electrode/electrolyte interfaces.[67,79] In its simplest form, the exchange process measured in EXSY can be described as the equilibrium between two sites as follows:

$$\text{site a} \underset{k_b}{\overset{k_a}{\rightleftharpoons}} \text{site b}$$

where k_a and k_b represent the forward and reverse rate constants, respectively, and the exchange rate constant, k_{ex}, is defined as $k_{ex} = k_a + k_b$. Exchange (either from chemical exchange or spin diffusion) between site 1 and site 2 manifests in a 2D EXSY experiment as a decrease in signal intensity along the diagonal and a simultaneous increase in signal intensity of crosspeak volume (Figure 2a) or simply a decrease in signal intensity in 1D EXSY as a function of mixing time (τ_{mix}). Variable temperature NMR experiments can be used to confirm that signal decay on the diagonal and/or increased crosspeak volume are the result of thermally-activated chemical exchange processes and not spin diffusion (a phenomena where magnetization spontaneously exchanges between two nearby sites due to the dipolar coupling between the two sites).[80] Our variable temperature 1D EXSY measurements performed at -20, 20, and 61 °C show a strong temperature dependence, indicating that the ^{7}Li-^{7}Li crosspeaks between Li metal and the SEI arise from chemical exchange and can be interpreted as such (Figures S16, S18).

2D ^{7}Li EXSY NMR results for the 0.5 M LiTFSI electrolyte are shown in Figure 3b and are used to assign the molecular pathways of exchange. Based on the crosspeaks in the SEI region, we see that Li exchange proceeds between individual Li-containing compounds in the SEI (Figure

3b: Li near ^{1}H (green), Li near ^{19}F (yellow), and Li_2O (blue)). Similar results are observed for 1 M LiTFSI (Figures S20a, i). Examination of the 1D row and column projections of the Li metal/SEI crosspeaks in pure LiTFSI electrolytes show exchange at the electrode/SEI interface is dominated by exchange across Li/Li_2O (Figures 3b, S20a, ii and vii). This data suggests that mostly Li from Li_2O is in contact with Li metal and is consistent with the reactive nature of Li metal. Even when stored under Ar, Li metal develops a layer of Li_2O that the SEI grows over (from any O_2 contamination).[81] The localization of Li_2O at the Li metal surface contrasts recent cryoEM reports showing crystalline Li_2O facing the electrolyte.[82] We hypothesize that exposure to liquid N_2 or UHV conditions may be responsible for these differences in SEI arrangement.[83]

For the $LiNO_3$-containing electrolyte, analysis of the 1D row projections of the SEI peak at the Li near H and Li near F peak positions (Figure S20g-h) indicates that the Li_2O contribution is negligible to the overall fit, suggesting that Li near fluorine (e.g., LiF) and Li near proton (e.g., organic lithium) environments in the SEI do not undergo significant chemical exchange with Li_2O when $LiNO_3$ is present. Depth-resolved XPS (Figure 4, right panel, LiTFSI/$LiNO_3$) shows growth of a N 1s orbital peak at 398.6 eV after 20 min of etching which is assigned to $Li_xN_yO_z$ from $LiNO_3$ decomposition. As $LiNO_3$ is readily reduced below 1.6 V vs Li^+/Li [61] it is likely these products deposit first on the native Li_2O layer on Li metal, physically suppressing chemical exchange between Li_2O and other SEI components. We note that when cycled in only LiTFSI, $Li_xN_yO_z$ species are not present, with the N 1s orbital region only showing a peak that corresponds to the nitrogen in $TFSI^-$ at approximately 399–400 eV (Figure 4, left panel, see SI for an expanded discussion of the XPS data). The lack of additional nitrate reduction products may allow both the organic and inorganic SEI to deposit on the Li_2O surface layer (e.g., the reduction potential of

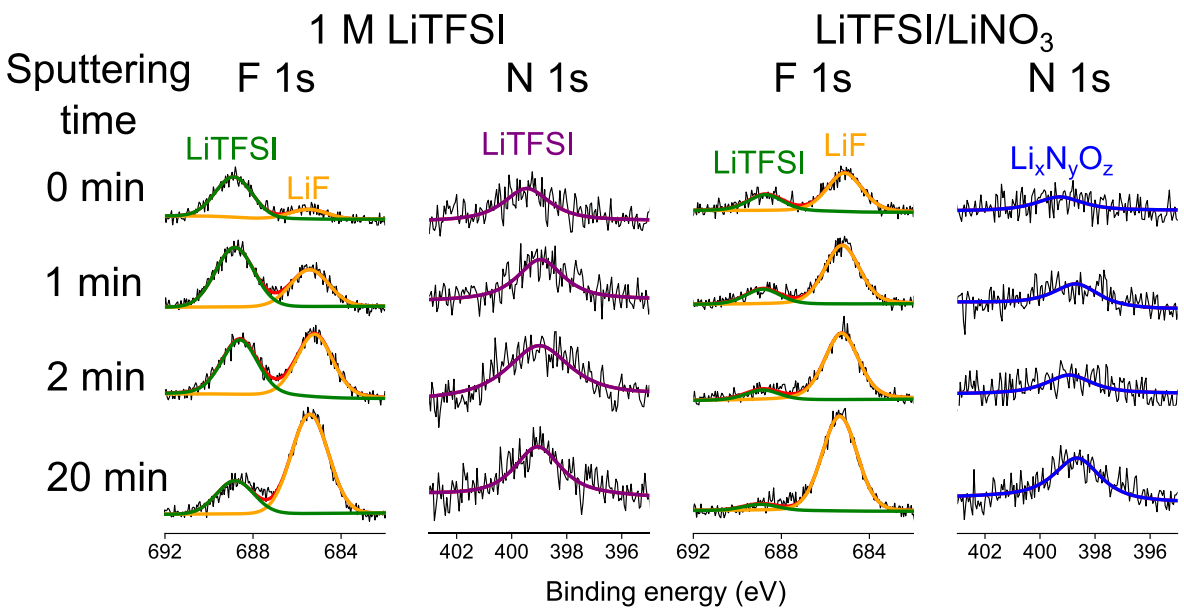

Figure 4. Depth-profiled F 1s and N 1s regions of XPS spectra of Li electrodes after 100 cycles at 1 mA cm^{-2} for 2 h cycles in 1 M LiTFSI (left) and 0.5 M LiTFSI + 0.5 M $LiNO_3$ (right). Time intervals on the leftmost panel denote total sputtering time. F 1s spectra are fitted and assigned to LiTFSI (green) and LiF (yellow), while N 1s spectra are fitted and assigned to LiTFSI (1 M LiTFSI, purple) and LixNyOz (LiTFSI/$LiNO_3$, blue). Red and black traces denote the composite spectrum fits and the raw data respectively. Spectra are referenced to adventitious carbon at 284.8 eV.

$TFSI^-$ is 1.4 V vs Li^+/Li[84]), consistent with the behavior observed in EXSY for both concentrations of LiTFSI electrolytes.

In order to measure the rate of Li exchange across individual interfaces assigned above, we performed a series of 1D EXSY experiments over a wide range of mixing times (τ_{mix} = 100 μs to 10 s, Figure 5). In the 1D experiment, we are able to monitor exchange in chemically-resolved regions of the ^7Li spectra because the exchanging components (e.g., Li metal and SEI) have different T_1 relaxation rates (Figure S13). The 1D EXSY decays corresponding to Li metal (264.5 ppm) and Li in the SEI (~0 ppm) are fit to a Bloch-McConnell two-site chemical exchange[85,86] model to extract the exchange rate constants. This model allows us to simultaneously account for the individual populations present during two-site exchange (P_{SEI} and P_{metal}), the fraction of that population undergoing exchange (f_{SEI} and f_{metal}), and T_1 relaxation (see SI for model details and fits to the experimental data).

We emphasize that each decay profile shown in Figure S16 represents the equilibrium chemical exchange rate across the interface of a given chemical environment and its neighbors.[75,87] The decay does not represent Li self-diffusion/site exchange within a bulk chemical environment or phase. Table 1 shows Li exchange rates from 1D EXSY analyses, as well as P_{SEI} and P_{metal}, f_{SEI}, and f_{metal}. The Li metal/SEI interfacial exchange rates in $LiNO_3$-containing electrolytes are at least twice as fast as those found in pure LiTFSI electrolytes. (N.B. the error bars for k_{ex} in Table 1 represent the standard error of the fitted variables, which heavily depend on the goodness-of-fit and the signal-to-noise ratio (SNR) SNR of the raw data. Thus, lower SNR NMR peaks exhibit higher standard errors). The increased exchange rate in the presence of $LiNO_3$ is correlated with the high CE values measured in Li/Cu cells. To determine whether this correlation holds under realistic operating conditions, EXSY experiments were also performed on Li metal anodes containing liquid electrolytes under static NMR conditions. We find that electrolyte ↔ SEI and SEI ↔ metal exchange in electrolyte-containing samples is slowest for the 0.5 M LiTFSI electrolyte, but similar between both 1 M LiTFSI and 0.5 M $LiNO_3$ + 0.5 M LiTFSI (Figure S17,

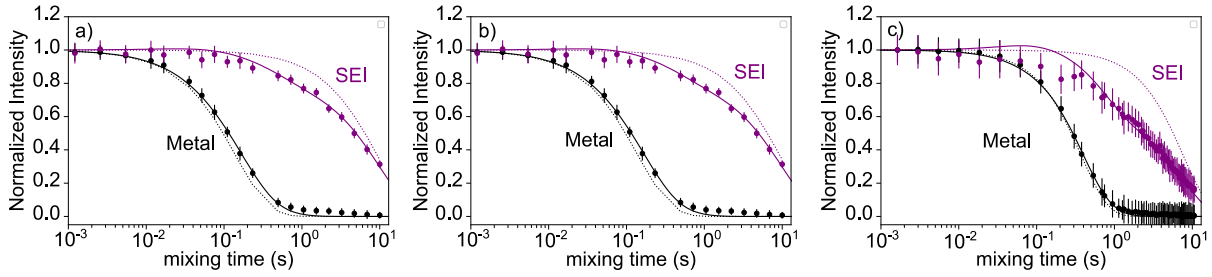

Figure 5. 1D ^{7}Li MAS EXSY raw data (circles) and Bloch-McConnell fits (solid lines) for Li metal (black) and the SEI (purple) formed in 0.5 M LiTFSI (a), 1 M LiTFSI (b), and 0.5 M LiTFSI + 0.5 M $LiNO_3$ (c). Intensities normalized to the first data point (τ_{mix} = 100 μs) are shown as a function of mixing time. Error bars represent 30× the standard deviation of the spectral noise. Dotted lines denote T_1 relaxation profiles using T_1 values from Figure S13, showing that chemical exchange occurs in all samples.

Table S3), suggesting that salt concentration plays an important role in dictating Li exchange across all interfaces.

In addition to rapid interfacial exchange, solution NMR analyses of the liquid electrolyte post-cycling indicate that more $TFSI^-$ decomposition occurs in pure LiTFSI electrolytes than in LiTFSI/$LiNO_3$ electrolytes. Comparison of the ^{19}F solution NMR for pristine and cycled electrolytes (Figure 6a) show large peaks at -79.4 ppm consistent with $TFSI^-$,[88] as well as small

Table 1. Chemical exchange rate constant between Li metal and the SEI (k_{ex}), SEI population (P_{SEI}), fraction of the SEI which undergoes exchange (f_{SEI}), and fraction of the Li metal which undergoes exchange (f_{metal}) based on Bloch-McConnell fits of MAS data shown in Figure S16 for 0.5 M LiTFSI, 1 M LiTFSI, and 0.5 M LiTFSI + 0.5 M $LiNO_3$. Error bars represent the standard error of the fitted variables and is dependent upon SNR in the NMR data.

Sample	**k_{ex} (s^{-1})**	**P_{SEI}**	**f_{SEI}**	**f_{metal}**
0.5 M LiTFSI	29.1 ± 21.9	0.58	0.17 ± 0.01	0.18 ± 0.07
1 M LiTFSI	5.5 ± 1.4	0.49	0.23 ± 0.01	0.29 ± 0.09
0.5 M LiTFSI + 0.5 M $LiNO_3$	80.6 ± 55.6	0.57	0.39 ± 0.01	0.17 ± 0.05

resonances at -79.1 ppm and -80 ppm which are assigned to $^{13}C/^{12}C$ isotope effects (i.e. $^{13}C\mathbf{F}_3SO_2NSO_2{}^{12}CF_3$, $^{12}C\mathbf{F}_3SO_2NSO_2{}^{13}CF_3$, and $^{12}C\mathbf{F}_3SO_2NSO_2{}^{12}CF_3$ will all exhibit different chemical shifts).[89] Resonances at -78.3 ppm, -78.4 ppm (0.2% of the sample), and -79.3 ppm (1.7% sample), which represent RCF_3 fragmentation are present in the cycled LiTFSI electrolytes, yet

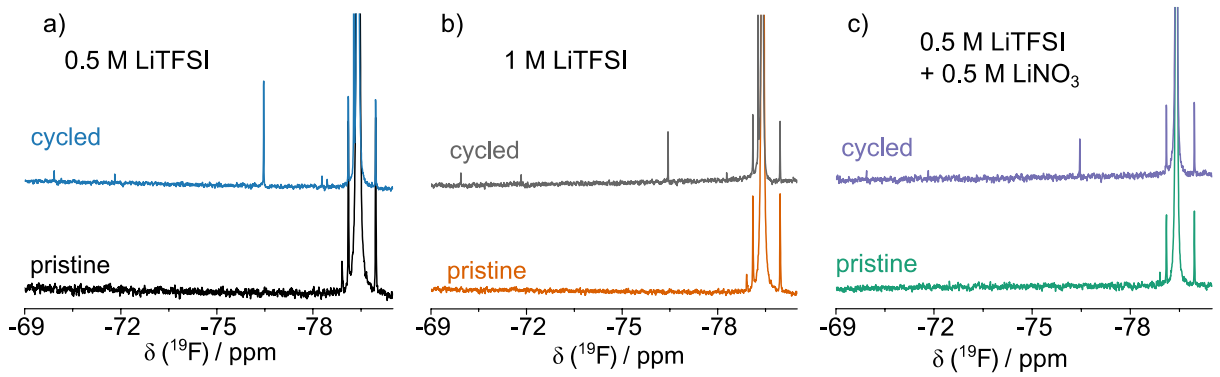

Figure 6. Solution ^{19}F NMR of pristine and cycled (100 cycles) DOL/DME electrolytes. a) 0.5 M LiTFSI; pristine is shown in blue and cycled is shown in grey. b) 1 M LiTFSI; pristine is shown in black and cycled is shown in orange. c) 0.5 M LiTFSI + 0.5 M $LiNO_3$; pristine is shown in green and cycled is shown in purple. The major resonance at -79.4 ppm assigned to $TFSI^-$ is cut off to highlight smaller peaks.

not in the cycled LiTFSI/$LiNO_3$ electrolyte, suggesting that $LiNO_3$ addition suppresses the electrolyte decomposition pathway that generates soluble $TFSI^-$ byproducts. As expected based on the electrochemical stability of ethers,[90] ^1H and ^{13}C solution NMR indicate that ether solvents show little to no decomposition during electrochemical cycling,[90] with the exception of a small amount of Li formate in LiTFSI electrolytes that does not form when $LiNO_3$ is present (Figures S3-S5).

Quantitative NMR and XPS suggest that the SEI in the presence of $LiNO_3$ is thicker and more heterogeneous than LiTFSI alone. Thus, the transition to smooth Li deposition morphologies and enhanced CE (Figure 1) must be predicated on rapid Li exchange across grain boundaries in the SEI in $LiNO_3$-based electrolytes. In other words, fast Li exchange in the SEI enabled by $LiNO_3$ decomposition (which leads to higher ionic conductivity across individual interfaces in the SEI and less solubility than those produced with LiTFSI alone) overrides the fact that the SEI is thicker and more heterogeneous in the presence of $LiNO_3$. This conclusion is in contrast to prevailing hypotheses that focus on performance-enhancing species such as $Li_xN_yO_z$ driving a more homogeneous SEI[13,47,51–56,62,91] and/or $LiNO_3$ reduction mitigating further electrolyte decomposition,[2,34] but is consistent with thicker SEIs observed in cryo-EM.[59] Importantly, the

mechanistic understanding of $LiNO_3$ performance enhancement provides a clear route to engineer future SEIs (either in situ or artificially).

Solution NMR from the current work (Figure 6), as well as our previous work,[48] show that performance-enhancing additives and bi-salts improve SEI stability in both carbonate and ethereal solvents by suppressing the formation of soluble compounds. At the same time, $LiNO_3$ addition to the electrolyte formulation increases both the rate of exchange and the fraction of the SEI which exchanges with the metal (Table 1), suggesting that deposited $Li_xN_yO_z$ products contribute to SEI ↔ metal exchange. Although the $LiNO_3$-containing electrolyte deposits a thicker SEI, it forms less non-conductive components (such as LiF[92,93]) than pure LiTFSI electrolytes, likely contributing to a higher interphasial ion conductivity. Strategies that encourage the formation of high-ionic conductivity SEI components *in situ* that simultaneously maintain stable SEI passivation on Li metal will be critical to improving Li^+ transport at the SEI/metal interface.

Our measurements indicate that the critical role of $LiNO_3$ in improving Li metal battery performance relies on modulating Li interfacial exchange between individual compounds in a heterogeneous SEI layer (e.g., between LiF and Li_2O). A combination of XPS and SSNMR show that when $LiNO_3$ is added to the electrolyte, $Li_xN_yO_z$ decomposition products form an additional passivation layer between Li_2O and the rest of the compounds in the SEI. Depth-resolved XPS shows that this $Li_xN_yO_z$ layer is intermixed with both organic and inorganic species in the SEI. High ionic conductivity $Li_xN_yO_z$ particles (e.g., Li_3N has an ionic conductivity of ~10^{-4} S/cm[94]) may provide fast Li^+ pathways between insulating LiF grains to alleviate the bottleneck in ion transport between the native Li_2O layer and the electrolyte. Grain boundaries between individual components in the SEI can also generate space-charge effects that can be used to control Li ion transport at the electrode/electrolyte interface.[95] As the exact composition and thus, chemical

potential of $Li_xN_yO_z$, is unknown, we speculate that $Li_xN_yO_z$ may tune the space-charge layer between individual grains in the SEI to improve Li ion transport in this region. Pan et al. have shown using DFT that the space charge layer effect created by heterogeneous grain boundaries (e.g. between LiF and Li_2CO_3) provides a chemical driving force for Li^+ transport across those interfaces.[96] Forming more of these heterogeneous grain boundaries through the use of readily oxidizing electrolyte additives such as $LiNO_3$, particularly those which form highly defective, ion-conducting reduction products on the Li metal surface, may be an effective route to improving Li ion transport at SEI/SEI interfaces. Taken together, our data suggest that modulating space-charge effects between grains in the SEI layer (e.g., through defect engineering[92]) may provide a promising route to achieving smooth Li deposition.[97–101]

Finally, measurements at the electrolyte/SEI interface show that Li ion transport in this region is dominated by electrolyte salt concentration. This insight may provide an additional explanation for the success of highly concentrated Li salts in Li metal batteries that affords another handle to tune Li deposition morphologies.[33,102–105] Interestingly, increasing electrolyte salt concentration is known to increase viscosity and hamper ionic conductivity in the bulk electrolyte;[103] instead, superconcentrated electrolytes are desired for their improved electrochemical stability in an expanded potential window. Our data suggest that increased salt concentration may also serve to improve Li^+ transport at the electrolyte/SEI interface.

In conclusion, a molecular-level understanding of Li^+ transport at electrolyte/SEI/electrolyte interfaces is key to designing high-performance electrolyte formulations. The SSNMR techniques presented here do not require isotopic enrichment and utilize simple NMR pulse sequences that are straightforward to set up and optimize for a wide range of samples. We speculate that tailoring electrolyte composition (to form an in situ SEI) or

designing an artificial SEI by focusing on engineering ionic conductivity will improve Li^+ transport across SEI interfaces, leading to smooth Li plating. SSNMR show that achieving a thin, chemically homogeneous SEI is not necessary for high CE (instead, the SEI should exhibit fast interfacial Li diffusion and low solubility), opening up new possibilities for successful SEI architectures.

ASSOCIATED CONTENT

Supporting Information. Experimental and modeling methods, auxiliary electrochemical cycling, solution NMR, SSNMR, model fits and fit parameters of T_1 inversion recovery data, variable mixing time EXSY data, and variable temperature EXSY data, and XPS

AUTHOR INFORMATION

Corresponding Author

Lauren E. Marbella—Department of Chemical Engineering, Columbia University, New York, New York 10027, United States; https://orcid.org/0000-0003-1639-391; email: lem2221@columbia.edu

Richard May—Department of Chemical Engineering, Columbia University, New York, New York 10027, United States; https://orcid.org/0000-0002-9478-0751

Keith J. Fritzsching—Department of Chemical Engineering, Columbia University, New York, New York 10027, United States; https://orcid.org/0000-0001-5486-614X

Dimitri Livitz—Department of Chemical Engineering, Columbia University, New York, New York 10027, United States; https://orcid.org/0000-0003-2528-1446

Steven R. Denny—Department of Chemical Engineering, Columbia University, New York, New York 10027, United States

Group website URL: https://www.marbella-lab.com/

Notes

The authors declare no competing financial interest.

ACKNOWLEDGMENT

This work was funded by the Alfred P. Sloan Foundation through a Scialog: Advanced Energy Storage Collaborative Innovation Award, (2019-11419). R.M. is supported by the U.S. Department of Defense through the National Defense Science & Engineering Graduate Fellowship (NDSEG) program. The authors thank Profs. Alan C. West and Dan Steingart for helpful discussions.

REFERENCES

(1) Zhang, S. S. Liquid Electrolyte Lithium/Sulfur Battery: Fundamental Chemistry, Problems, and Solutions. *J. Power Sources* **2013**, *231*, 153–162. https://doi.org/10.1016/j.jpowsour.2012.12.102.

(2) Aurbach, D.; Pollak, E.; Elazari, R.; Salitra, G.; Kelley, C. S.; Affinito, J. On the Surface Chemical Aspects of Very High Energy Density, Rechargeable Li–Sulfur Batteries. *J. Electrochem. Soc.* **2009**, *156*, A694–A702. https://doi.org/10.1149/1.3148721.

(3) Girishkumar, G.; McCloskey, B.; Luntz, A. C.; Swanson, S.; Wilcke, W. Lithium-Air Battery: Promise and Challenges. *J. Phys. Chem. Lett.* **2010**, *1*, 2193–2203.

(4) Aurbach, D.; McCloskey, B. D.; Nazar, L. F.; Bruce, P. G. Advances in Understanding Mechanisms Underpinning Lithium-Air Batteries. *Nat. Energy* **2016**, *1*, 1–11. https://doi.org/10.1038/nenergy.2016.128.

(5) Lu, Y. C.; Gallant, B. M.; Kwabi, D. G.; Harding, J. R.; Mitchell, R. R.; Whittingham, M. S.; Shao-Horn, Y. Lithium-Oxygen Batteries: Bridging Mechanistic Understanding and Battery Performance. *Energy Environ. Sci.* **2013**, *6*, 750–768. https://doi.org/10.1039/c3ee23966g.

(6) Mitchell, R. R.; Gallant, B. M.; Thompson, C. V.; Shao-Horn, Y. All-Carbon-Nanofiber Electrodes for High-Energy Rechargeable Li-O 2 Batteries. *Energy Environ. Sci.* **2011**, *4*, 2952–2958. https://doi.org/10.1039/c1ee01496j.

(7) Janek, J.; Zeier, W. G. A Solid Future for Battery Development. *Nat. Energy* **2016**, *1*, 1–4. https://doi.org/10.1038/nenergy.2016.141.

(8) Zhao, Q.; Liu, X.; Stalin, S.; Khan, K.; Archer, L. A. Solid-State Polymer Electrolytes with in-Built Fast Interfacial Transport for Secondary Lithium Batteries. *Nat. Energy* **2019**, *4*, 365–373. https://doi.org/10.1038/s41560-019-0349-7.

(9) Rangasamy, E.; Wolfenstine, J.; Sakamoto, J. The Role of Al and Li Concentration on the Formation of Cubic Garnet Solid Electrolyte of Nominal Composition Li 7La 3Zr 2O 12. *Solid State Ionics* **2012**, *206*, 28–32. https://doi.org/10.1016/j.ssi.2011.10.022.

(10) Zheng, J.; Hu, Y. Y. New Insights into the Compositional Dependence of Li-Ion Transport in Polymer-Ceramic Composite Electrolytes. *ACS Appl. Mater. Interfaces* **2018**, *10*, 4113–4120. https://doi.org/10.1021/acsami.7b17301.

(11) Leube, B. T.; Inglis, K. K.; Carrington, E. J.; Sharp, P. M.; Shin, J. F.; Neale, A. R.; Manning, T. D.; Pitcher, M. J.; Hardwick, L. J.; Dyer, M. S.; Blanc, F.; Claridge, J. B.; Rosseinsky, M. J. Lithium Transport in Li4.4 M0.4 M′0.6S4 (M = Al3+, Ga3+, and M′ = Ge4+, Sn4+): Combined Crystallographic, Conductivity, Solid State NMR, and Computational Studies. *Chem. Mater.* **2018**, *30*, 7183–7200. https://doi.org/10.1021/acs.chemmater.8b03175.

(12) Bai, P.; Li, J.; Brushett, F. R.; Bazant, M. Z. Transition of Lithium Growth Mechanisms in Liquid Electrolytes. *Energy Environ. Sci.* **2016**, *9*, 3221–3229. https://doi.org/10.1039/C6EE01674J.

(13) Fang, C.; Wang, X.; Meng, Y. S. Key Issues Hindering a Practical Lithium-Metal Anode. *Trends Chem.* **2019**, *1*, 152–158. https://doi.org/10.1016/j.trechm.2019.02.015.

(14) Wood, K. N.; Noked, M.; Dasgupta, N. P. Lithium Metal Anodes: Toward an Improved Understanding of Coupled Morphological, Electrochemical, and Mechanical Behavior. *ACS Energy Lett.* **2017**, *2*, 664–672. https://doi.org/10.1021/acsenergylett.6b00650.

(15) Liu, J.; Bao, Z.; Cui, Y.; Dufek, E. J.; Goodenough, J. B.; Khalifah, P.; Li, Q.; Liaw, B. Y.; Liu, P.; Manthiram, A.; Meng, Y. S.; Subramanian, V. R.; Toney, M. F.; Viswanathan, V.

V.; Whittingham, M. S.; Xiao, J.; Xu, W.; Yang, J.; Yang, X. Q.; Zhang, J. G. Pathways for Practical High-Energy Long-Cycling Lithium Metal Batteries. *Nat. Energy* **2019**, *4*, 180–186.

(16) Lu, D.; Shao, Y.; Lozano, T.; Bennett, W. D.; Graff, G. L.; Polzin, B.; Zhang, J.; Engelhard, M. H.; Saenz, N. T.; Henderson, W. A.; Bhattacharya, P.; Liu, J.; Xiao, J. Failure Mechanism for Fast-Charged Lithium Metal Batteries with Liquid Electrolytes. *Adv. Energy Mater.* **2015**, *5*, 1400993. https://doi.org/10.1002/aenm.201400993.

(17) Bhattacharyya, R.; Key, B.; Chen, H.; Best, A. S.; Hollenkamp, A. F.; Grey, C. P. In Situ NMR Observation of the Formation of Metallic Lithium Microstructures in Lithium Batteries. *Nat. Mater.* **2010**, *9*, 504–510. https://doi.org/10.1038/nmat2764.

(18) Chen, K. H.; Wood, K. N.; Kazyak, E.; Lepage, W. S.; Davis, A. L.; Sanchez, A. J.; Dasgupta, N. P. Dead Lithium: Mass Transport Effects on Voltage, Capacity, and Failure of Lithium Metal Anodes. *J. Mater. Chem. A* **2017**, *5*, 11671–11681. https://doi.org/10.1039/c7ta00371d.

(19) Wood, K. N.; Kazyak, E.; Chadwick, A. F.; Chen, K. H.; Zhang, J. G.; Thornton, K.; Dasgupta, N. P. Dendrites and Pits: Untangling the Complex Behavior of Lithium Metal Anodes through Operando Video Microscopy. *ACS Cent. Sci.* **2016**, *11*, 790–801. https://doi.org/10.1021/acscentsci.6b00260.

(20) Marbella, L. E.; Zekoll, S.; Kasemchainan, J.; Emge, S. P.; Bruce, P. G.; Grey, C. P. 7 Li NMR Chemical Shift Imaging to Detect Microstructural Growth of Lithium in All-Solid-State Batteries. *Chem. Mater.* **2019**, *31*, 2762–2769. https://doi.org/10.1021/acs.chemmater.8b04875.

(21) Tikekar, M. D.; Choudhury, S.; Tu, Z.; Archer, L. A. Design Principles for Electrolytes and Interfaces for Stable Lithium-Metal Batteries. *Nat. Energy* **2016**, *1*, 16114. https://doi.org/10.1038/nenergy.2016.114.

(22) Pei, A.; Zheng, G.; Shi, F.; Li, Y.; Cui, Y. Nanoscale Nucleation and Growth of Electrodeposited Lithium Metal. *Nano Lett.* **2017**, *17*, 1132–1139.

https://doi.org/10.1021/acs.nanolett.6b04755.

(23) Peled, E. The Electrochemical Behavior of Alkali and Alkaline Earth Metals in Nonaqueous Battery Systems—The Solid Electrolyte Interphase Model. *J. Electrochem. Soc.* **1979**, *126*, 2047. https://doi.org/10.1149/1.2128859.

(24) Cheng, X. B.; Zhang, R.; Zhao, C. Z.; Wei, F.; Zhang, J. G.; Zhang, Q. A Review of Solid Electrolyte Interphases on Lithium Metal Anode. *Adv. Sci.* **2015**, *3*, 1–20. https://doi.org/10.1002/advs.201500213.

(25) Hao, F.; Verma, A.; Mukherjee, P. P. Mechanistic Insight into Dendrite-SEI Interactions for Lithium Metal Electrodes. *J. Mater. Chem. A* **2018**, *6*, 19664–19671. https://doi.org/10.1039/c8ta07997h.

(26) Kazyak, E.; Wood, K. N.; Dasgupta, N. P. Improved Cycle Life and Stability of Lithium Metal Anodes through Ultrathin Atomic Layer Deposition Surface Treatments. *Chem. Mater.* **2015**, *18*, 6457–6462. https://doi.org/10.1021/acs.chemmater.5b02789.

(27) Lv, S.; Verhallen, T.; Vasileiadis, A.; Ooms, F.; Xu, Y.; Li, Z.; Li, Z.; Wagemaker, M. Operando Monitoring the Lithium Spatial Distribution of Lithium Metal Anodes. *Nat. Commun.* **2018**, *9*, 2152. https://doi.org/10.1038/s41467-018-04394-3.

(28) Bieker, G.; Winter, M.; Bieker, P. Electrochemical in Situ Investigations of SEI and Dendrite Formation on the Lithium Metal Anode. *Phys. Chem. Chem. Phys.* **2015**, *17*, 8670–8679. https://doi.org/10.1039/c4cp05865h.

(29) Cohen, Y. S.; Cohen, Y.; Aurbach, D. Micromorphological Studies of Lithium Electrodes in Alkyl Carbonate Solutions Using in Situ Atomic Force Microscopy. *J. Phys. Chem. B* **2000**, *104*, 12282–12291. https://doi.org/10.1021/jp002526b.

(30) Fang, C.; Li, J.; Zhang, M.; Zhang, Y.; Yang, F.; Lee, J. Z.; Lee, M.-H.; Alvarado, J.; Schroeder, M. A.; Yang, Y.; Lu, B.; Williams, N.; Ceja, M.; Yang, L.; Cai, M.; Gu, J.; Xu, K.; Wang, X.; Meng, Y. S. Quantifying Inactive Lithium in Lithium Metal Batteries. *Nature* **2019**, *572*, 511–515. https://doi.org/10.1038/s41586-019-1481-z.

(31) Chandrashekar, S.; Trease, N. M.; Chang, H. J.; Du, L. S.; Grey, C. P.; Jerschow, A. 7Li MRI of Li Batteries Reveals Location of Microstructural Lithium. *Nat. Mater.* **2012**, *11*, 311–315. https://doi.org/10.1038/nmat3246.

(32) Ilott, A. J.; Mohammadi, M.; Chang, H. J.; Grey, C. P.; Jerschow, A. Real-Time 3D Imaging of Microstructure Growth in Battery Cells Using Indirect MRI. *Proc. Natl. Acad. Sci.* **2016**. https://doi.org/10.1073/pnas.1607903113.

(33) Qian, J.; Henderson, W. A.; Xu, W.; Bhattacharya, P.; Engelhard, M.; Borodin, O.; Zhang, J. G. High Rate and Stable Cycling of Lithium Metal Anode. *Nat. Commun.* **2015**, *6*, 6362. https://doi.org/10.1038/ncomms7362.

(34) Li, W.; Yao, H.; Yan, K.; Zheng, G.; Liang, Z.; Chiang, Y. M.; Cui, Y. The Synergetic Effect of Lithium Polysulfide and Lithium Nitrate to Prevent Lithium Dendrite Growth. *Nat. Commun.* **2015**, *6*, 7436. https://doi.org/10.1038/ncomms8436.

(35) Suo, L.; Xue, W.; Gobet, M.; Greenbaum, S. G.; Wang, C.; Chen, Y.; Yang, W.; Li, Y.; Li, J. Fluorine-Donating Electrolytes Enable Highly Reversible 5-V-Class Li Metal Batteries. *Proc. Natl. Acad. Sci.* **2018**, *115*, 1156–1161. https://doi.org/10.1073/pnas.1712895115.

(36) Xu, W.; Wang, J.; Ding, F.; Chen, X.; Nasybulin, E.; Zhang, Y.; Zhang, J. G. Lithium Metal Anodes for Rechargeable Batteries. *Energy Environ. Sci.* **2014**, *7*, 513. https://doi.org/10.1039/c3ee40795k.

(37) Mehdi, B. L.; Stevens, A.; Qian, J.; Park, C.; Xu, W.; Henderson, W. A.; Zhang, J. G.; Mueller, K. T.; Browning, N. D. The Impact of Li Grain Size on Coulombic Efficiency in Li Batteries. *Sci. Rep.* **2016**, *6*, 34267. https://doi.org/10.1038/srep34267.

(38) Zhang, X. Q.; Cheng, X. B.; Chen, X.; Yan, C.; Zhang, Q. Fluoroethylene Carbonate Additives to Render Uniform Li Deposits in Lithium Metal Batteries. *Adv. Funct. Mater.* **2017**, *27*, 1605989. https://doi.org/10.1002/adfm.201605989.

(39) Cheng, X. B.; Hou, T. Z.; Zhang, R.; Peng, H. J.; Zhao, C. Z.; Huang, J. Q.; Zhang, Q. Dendrite-Free Lithium Deposition Induced by Uniformly Distributed Lithium Ions for Efficient Lithium Metal Batteries. *Adv. Mater.* **2016**, *28*, 2888–2895.

https://doi.org/10.1002/adma.201506124.

(40) Gofer, Y.; Ben-Zion, M.; Aurbach, D. Solutions of LiAsF6 in 1,3-Dioxolane for Secondary Lithium Batteries. *J. Power Sources* **1992**, *39*, 163–178. https://doi.org/10.1016/0378-7753(92)80135-X.

(41) Harry, K. J.; Hallinan, D. T.; Parkinson, D. Y.; MacDowell, A. A.; Balsara, N. P. Detection of Subsurface Structures underneath Dendrites Formed on Cycled Lithium Metal Electrodes. *Nat. Mater.* **2014**, *13*, 69–73. https://doi.org/10.1038/nmat3793.

(42) Sudo, R.; Nakata, Y.; Ishiguro, K.; Matsui, M.; Hirano, A.; Takeda, Y.; Yamamoto, O.; Imanishi, N. Interface Behavior between Garnet-Type Lithium-Conducting Solid Electrolyte and Lithium Metal. *Solid State Ionics* **2014**, *262*, 151–154. https://doi.org/10.1016/j.ssi.2013.09.024.

(43) Ren, Y.; Shen, Y.; Lin, Y.; Nan, C. W. Direct Observation of Lithium Dendrites inside Garnet-Type Lithium-Ion Solid Electrolyte. *Electrochem. commun.* **2015**, *57*, 27–30. https://doi.org/10.1016/j.elecom.2015.05.001.

(44) Kasemchainan, J.; Zekoll, S.; Spencer Jolly, D.; Ning, Z.; Hartley, G. O.; Marrow, J.; Bruce, P. G. Critical Stripping Current Leads to Dendrite Formation on Plating in Lithium Anode Solid Electrolyte Cells. *Nat. Mater.* **2019**, *18*, 1105–1111. https://doi.org/10.1038/s41563-019-0438-9.

(45) Bhowmik, A.; Castelli, I. E.; Garcia-Lastra, J. M.; Jørgensen, P. B.; Winther, O.; Vegge, T. A Perspective on Inverse Design of Battery Interphases Using Multi-Scale Modelling, Experiments and Generative Deep Learning. *Energy Storage Mater.* **2019**, *21*, 446–456. https://doi.org/10.1016/j.ensm.2019.06.011.

(46) Zhao, Q.; Tu, Z.; Wei, S.; Zhang, K.; Choudhury, S.; Liu, X.; Archer, L. A. Building Organic/Inorganic Hybrid Interphases for Fast Interfacial Transport in Rechargeable Metal Batteries. *Angew. Chemie - Int. Ed.* **2018**, *130*, 1004–1008. https://doi.org/10.1002/anie.201711598.

(47) Chandrasiri, K. W. D. K.; Nguyen, C. C.; Zhang, Y.; Parimalam, B. S.; Lucht, B. L.

Systematic Investigation of Alkali Metal Ions as Additives for Graphite Anode in Propylene Carbonate Based Electrolytes. *Electrochim. Acta* **2017**, *250*, 285–291. https://doi.org/10.1016/j.electacta.2017.08.065.

(48) May, R.; Zhang, Y.; Denny, S. R.; Viswanathan, V.; Marbella, L. E. Leveraging Cation Identity to Engineer Solid Electrolyte Interphases for Rechargeable Lithium Metal Anodes. *Cell Reports Phys. Sci.* **2020**, *1*, 1–16. https://doi.org/10.1016/j.xcrp.2020.100239.

(49) Goodenough, J. B.; Kim, Y. Challenges for Rechargeable Li Batteries. *Chem. Mater.* **2010**, *22*, 587–603. https://doi.org/10.1021/cm901452z.

(50) Yan, K.; Lee, H. W.; Gao, T.; Zheng, G.; Yao, H.; Wang, H.; Lu, Z.; Zhou, Y.; Liang, Z.; Liu, Z.; Chu, S.; Cui, Y. Ultrathin Two-Dimensional Atomic Crystals as Stable Interfacial Layer for Improvement of Lithium Metal Anode. *Nano Lett.* **2014**, *14*, 6016–6022. https://doi.org/10.1021/nl503125u.

(51) Jurng, S.; Brown, Z. L.; Kim, J.; Lucht, B. L. Effect of Electrolyte on the Nanostructure of the Solid Electrolyte Interphase (SEI) and Performance of Lithium Metal Anodes. *Energy Environ. Sci.* **2018**, *11*, 2600–2608. https://doi.org/10.1039/c8ee00364e.

(52) Wondimkun, Z. T.; Beyene, T. T.; Weret, M. A.; Sahalie, N. A.; Huang, C. J.; Thirumalraj, B.; Jote, B. A.; Wang, D.; Su, W. N.; Wang, C. H.; Brunklaus, G.; Winter, M.; Hwang, B. J. Binder-Free Ultra-Thin Graphene Oxide as an Artificial Solid Electrolyte Interphase for Anode-Free Rechargeable Lithium Metal Batteries. *J. Power Sources* **2020**, *450*, 227589. https://doi.org/10.1016/j.jpowsour.2019.227589.

(53) KUWATA, H.; SONOKI, H.; MATSUI, M.; MATSUDA, Y.; IMANISHI, N. Surface Layer and Morphology of Lithium Metal Electrodes. *Electrochemistry* **2016**, *84*, 854–860. https://doi.org/10.5796/electrochemistry.84.854.

(54) Zhang, J.; Wang, D. W.; Lv, W.; Zhang, S.; Liang, Q.; Zheng, D.; Kang, F.; Yang, Q. H. Achieving Superb Sodium Storage Performance on Carbon Anodes through an Ether-Derived Solid Electrolyte Interphase. *Energy Environ. Sci.* **2017**, *10*, 370–376. https://doi.org/10.1039/c6ee03367a.

(55) Luo, J.; Fang, C. C.; Wu, N. L. High Polarity Poly(Vinylidene Difluoride) Thin Coating for Dendrite-Free and High-Performance Lithium Metal Anodes. *Adv. Energy Mater.* **2018**, *8*, 1701482. https://doi.org/10.1002/aenm.201701482.

(56) Gu, Y.; Wang, W. W.; Li, Y. J.; Wu, Q. H.; Tang, S.; Yan, J. W.; Zheng, M. Sen; Wu, D. Y.; Fan, C. H.; Hu, W. Q.; Chen, Z. Bin; Fang, Y.; Zhang, Q. H.; Dong, Q. F.; Mao, B. W. Designable Ultra-Smooth Ultra-Thin Solid-Electrolyte Interphases of Three Alkali Metal Anodes. *Nat. Commun.* **2018**, *9*, 1339. https://doi.org/10.1038/s41467-018-03466-8.

(57) Wu, C. M.; Saravanan, L.; Chen, H. Y.; Pan, P. I.; Tsao, C. S.; Chang, C. C. Solid Electrolyte Interphase Layer Formation on Mesophase Graphite Electrodes with Different Electrolytes Studied by Small-Angle Neutron Scattering. *J. Chinese Chem. Soc.* **2020**, 1–10. https://doi.org/10.1002/jccs.202000480.

(58) Cao, C.; Abate, I. I.; Sivonxay, E.; Shyam, B.; Jia, C.; Moritz, B.; Devereaux, T. P.; Persson, K. A.; Steinrück, H. G.; Toney, M. F. Solid Electrolyte Interphase on Native Oxide-Terminated Silicon Anodes for Li-Ion Batteries. *Joule* **2019**, *3*, 762–781. https://doi.org/10.1016/j.joule.2018.12.013.

(59) Lin, D.; Liu, Y.; Li, Y.; Li, Y.; Pei, A.; Xie, J.; Huang, W.; Cui, Y. Fast Galvanic Lithium Corrosion Involving a Kirkendall-Type Mechanism. *Nat. Chem.* **2019**, *11*, 382–389. https://doi.org/10.1038/s41557-018-0203-8.

(60) Park, K.; Goodenough, J. B. Dendrite-Suppressed Lithium Plating from a Liquid Electrolyte via Wetting of Li3N. *Adv. Energy Mater.* **2017**, *7*, 1700732. https://doi.org/10.1002/aenm.201700732.

(61) Zhang, S. S. Role of LiNO 3 in Rechargeable Lithium/Sulfur Battery. *Electrochim. Acta* **2012**, *70*, 344–348. https://doi.org/10.1016/j.electacta.2012.03.081.

(62) Xiong, S.; Xie, K.; Diao, Y.; Hong, X. Properties of Surface Film on Lithium Anode with LiNO3 as Lithium Salt in Electrolyte Solution for Lithium-Sulfur Batteries. *Electrochim. Acta* **2012**, *83*, 78–86. https://doi.org/10.1016/j.electacta.2012.07.118.

(63) Rosy; Akabayov, S.; Leskes, M.; Noked, M. Bifunctional Role of LiNO3 in Li-O2 Batteries:

Deconvoluting Surface and Catalytic Effects. *ACS Appl. Mater. Interfaces* **2018**, *10*, 29622–29629. https://doi.org/10.1021/acsami.8b10054.

(64) Jeener, J.; Meier, B. H.; Bachmann, P.; Ernst, R. R. Investigation of Exchange Processes by Two-Dimensional NMR Spectroscopy. *J. Chem. Phys.* **1979**, *71*, 4546. https://doi.org/10.1063/1.438208.

(65) Smiley, D. L.; Goward, G. R. Solid-State NMR Studies of Chemical Exchange in Ion Conductors for Alternative Energy Applications. *Concepts Magn. Reson. Part A Bridg. Educ. Res.* **2016**, *45A*, e21419. https://doi.org/10.1002/cmr.a.21419.

(66) Bottke, P.; Freude, D.; Wilkening, M. Ultraslow Li Exchange Processes in Diamagnetic Li2ZrO 3 as Monitored by EXSY NMR. *J. Phys. Chem. C* **2013**, *16*, 8114–8119. https://doi.org/10.1021/jp401350u.

(67) Wagemaker, M.; Kentjens, A. P. M.; Mulder, F. M. Equilibrium Lithium Transport between Nanocrystalline Phases in Intercalated TiO2 Anatase. *Nature* **2002**, *418*, 397–399. https://doi.org/10.1038/nature00901.

(68) Davis, L. J. M.; Ellis, B. L.; Ramesh, T. N.; Nazar, L. F.; Bain, A. D.; Goward, G. R. 6Li 1D EXSY NMR Spectroscopy: A New Tool for Studying Lithium Dynamics in Paramagnetic Materials Applied to Monoclinic Li2VPO 4F. *J. Phys. Chem. C* **2011**, *115*, 22603–22608. https://doi.org/10.1021/jp2059408.

(69) Cahill, L. S.; Chapman, R. P.; Britten, J. F.; Goward, G. R. 7Li NMR and Two-Dimensional Exchange Study of Lithium Dynamics in Monoclinic Li3v2(PO4)3. *J. Phys. Chem. B* **2006**, *14*, 7171–7177. https://doi.org/10.1021/jp057015+.

(70) Schmidt, W.; Wilkening, M. Discriminating the Mobile Ions from the Immobile Ones in Li4+xTi5O12: 6Li NMR Reveals the Main Li+ Diffusion Pathway and Proposes a Refined Lithiation Mechanism. *J. Phys. Chem. C* **2016**, *21*, 11372–11381. https://doi.org/10.1021/acs.jpcc.6b02828.

(71) Witt, E.; Chandran, C. V.; Heitjans, P. Slow Ion Exchange in Crystalline Li2SO4 ·H2OA 6Li 2D EXSY NMR Investigation. *Solid State Ionics* **2017**, *304*, 60–64.

https://doi.org/10.1016/j.ssi.2017.03.016.

(72) Zheng, J.; Tang, M.; Hu, Y. Y. Lithium Ion Pathway within Li7La3Zr2O12-Polyethylene Oxide Composite Electrolytes. *Angew. Chemie - Int. Ed.* **2016**, *128*, 12726–12730. https://doi.org/10.1002/anie.201607539.

(73) Davis, L. J. M.; Heinmaa, I.; Goward, G. R. Study of Lithium Dynamics in Monoclinic Li3Fe 2(PO4)3 Using 6Li VT and 2D Exchange MAS NMR Spectroscopy. *Chem. Mater.* **2010**, *22*, 769–775. https://doi.org/10.1021/cm901402u.

(74) Cahill, L. S.; Chapman, R. P.; Kirby, C. W.; Goward, G. R. The Challenge of Paramagnetism in Two-Dimensional 6,7Li Exchange NMR. *Appl. Magn. Reson.* **2007**, *32*, 565–581. https://doi.org/10.1007/s00723-007-0046-8.

(75) Ganapathy, S.; Yu, C.; Van Eck, E. R. H.; Wagemaker, M. Peeking across Grain Boundaries in a Solid-State Ionic Conductor. *ACS Energy Lett.* **2019**, *4*, 1092−1097. https://doi.org/10.1021/acsenergylett.9b00610.

(76) Cheng, Z.; Liu, M.; Ganapathy, S.; Li, C.; Li, Z.; Zhang, X.; He, P.; Zhou, H.; Wagemaker, M. Revealing the Impact of Space-Charge Layers on the Li-Ion Transport in All-Solid-State Batteries. *Joule* **2020**, *4*, 1311–1323. https://doi.org/10.1016/j.joule.2020.04.002.

(77) Yu, C.; Ganapathy, S.; Van Eck, E. R. H.; Van Eijck, L.; Basak, S.; Liu, Y.; Zhang, L.; Zandbergen, H. W.; Wagemaker, M. Revealing the Relation between the Structure, Li-Ion Conductivity and Solid-State Battery Performance of the Argyrodite Li6PS5Br Solid Electrolyte. *J. Mater. Chem. A* **2017**, *5*, 21178–21188. https://doi.org/10.1039/c7ta05031c.

(78) Yu, C.; Ganapathy, S.; Eck, E. R. H. V.; Wang, H.; Basak, S.; Li, Z.; Wagemaker, M. Accessing the Bottleneck in All-Solid State Batteries, Lithium-Ion Transport over the Solid-Electrolyte-Electrode Interface. *Nat. Commun.* **2017**, *8*, 1086. https://doi.org/10.1038/s41467-017-01187-y.

(79) Ganapathy, S.; Vanâ; Kentgens, A. P. M.; Mulder, F. M.; Wagemaker, M. Equilibrium Lithium-Ion Transport between Nanocrystalline Lithium-Inserted Anatase TiO 2 and the Electrolyte. *Chem. - A Eur. J.* **2011**, *17*, 14811–14816.

https://doi.org/10.1002/chem.201101431.

(80) Xu, Z.; Stebbins, J. F. Cation Dynamics and Diffusion in Lithium Orthosilicate: Two-Dimensional Lithium-6 NMR. *Science (80-.).* **1995**, *270*, 1332–1334. https://doi.org/10.1126/science.270.5240.1332.

(81) Kanamura, K.; Takezawa, H.; Shiraishi, S.; Takehara, Z. Chemical Reaction of Lithium Surface during Immersion in LiClO4 or LiPF6 / DEC Electrolyte. *J. Electrochem. Soc.* **1997**, *144*, 1900–1906. https://doi.org/10.1149/1.1837718.

(82) Thenuwara, A. C.; Shetty, P. P.; McDowell, M. T. Distinct Nanoscale Interphases and Morphology of Lithium Metal Electrodes Operating at Low Temperatures. *Nano Lett.* **2019**, *19*, 8664−8672. https://doi.org/10.1021/acs.nanolett.9b03330.

(83) Desimoni, E.; Casella, G. I.; Salvi, A. M.; Cataldi, T. R. I.; Morone, A. XPS Investigation of Ultra-High-Vacuum Storage Effects on Carbon Fibre Surfaces. *Carbon N. Y.* **1992**, *30*, 527–531. https://doi.org/10.1016/0008-6223(92)90171-R.

(84) Wang, A.; Kadam, S.; Li, H.; Shi, S.; Qi, Y. Review on Modeling of the Anode Solid Electrolyte Interphase (SEI) for Lithium-Ion Batteries. *npj Comput. Mater.* **2018**, *4*, 15. https://doi.org/10.1038/s41524-018-0064-0.

(85) McConnell, H. M. Reaction Rates by Nuclear Magnetic Resonance. *J. Chem. Phys.* **1958**, *28*, 430. https://doi.org/10.1063/1.1744152.

(86) Abergel, D.; Palmer, A. G. Approximate Solutions of the Bloch-McConnell Equations Chemical Equations for Two-Site Chemical Exchange. *ChemPhysChem* **2004**, *5*, 787–793. https://doi.org/10.1002/cphc.200301051.

(87) Haber, S.; Leskes, M. What Can We Learn from Solid State NMR on the Electrode–Electrolyte Interface? *Adv. Mater.* **2018**, *30*, 1706496. https://doi.org/10.1002/adma.201706496.

(88) Parimalam, B. S.; Lucht, B. L. Reduction Reactions of Electrolyte Salts for Lithium Ion Batteries: LiPF 6 , LiBF 4 , LiDFOB, LiBOB, and LiTFSI. *J. Electrochem. Soc.* **2018**, *165*,

A251–A255. https://doi.org/10.1149/2.0901802jes.

(89) Foris, A. 37,35Cl Isotope Effects on 19F and 13C Chemical Shifts of Chlorofluoro- and Hydrochlorofluorocarbons. *Magn. Reson. Chem.* **2000**, *38*, 813–819. https://doi.org/10.1002/1097-458x(200010)38:10<813::aid-mrc669>3.3.co;2-n.

(90) Winter, M.; Barnett, B.; Xu, K. Before Li Ion Batteries. *Chem. Rev.* **2018**, *118* (23), 11433–11456. https://doi.org/10.1021/acs.chemrev.8b00422.

(91) Zhang, X. Q.; Chen, X.; Cheng, X. B.; Li, B. Q.; Shen, X.; Yan, C.; Huang, J. Q.; Zhang, Q. Highly Stable Lithium Metal Batteries Enabled by Regulating the Solvation of Lithium Ions in Nonaqueous Electrolytes. *Angew. Chemie - Int. Ed.* **2018**, *57*, 5301 –5305. https://doi.org/10.1002/anie.201801513.

(92) Pan, J.; Cheng, Y. T.; Qi, Y. General Method to Predict Voltage-Dependent Ionic Conduction in a Solid Electrolyte Coating on Electrodes. *Phys. Rev. B - Condens. Matter Mater. Phys.* **2015**, *91*, 134116. https://doi.org/10.1103/PhysRevB.91.134116.

(93) Yildirim, H.; Kinaci, A.; Chan, M. K. Y.; Greeley, J. P. First-Principles Analysis of Defect Thermodynamics and Ion Transport in Inorganic SEI Compounds: LiF and NaF. *ACS Appl. Mater. Interfaces* **2015**, *7*, 18985–18996. https://doi.org/10.1021/acsami.5b02904.

(94) Boukamp, B. A.; Huggins, R. A. Fast Ionic Conductivity in Lithium Nitride. *Mater. Res. Bull.* **1978**, *13*, 23–32. https://doi.org/10.1016/0025-5408(78)90023-5.

(95) Zhang, Q.; Pan, J.; Lu, P.; Liu, Z.; Verbrugge, M. W.; Sheldon, B. W.; Cheng, Y. T.; Qi, Y.; Xiao, X. Synergetic Effects of Inorganic Components in Solid Electrolyte Interphase on High Cycle Efficiency of Lithium Ion Batteries. *Nano Lett.* **2016**, *16*, 2011−2016. https://doi.org/10.1021/acs.nanolett.5b05283.

(96) Pan, J.; Zhang, Q.; Xiao, X.; Cheng, Y. T.; Qi, Y. Design of Nanostructured Heterogeneous Solid Ionic Coatings through a Multiscale Defect Model. *ACS Appl. Mater. Interfaces* **2016**, *8*, 5687–5693. https://doi.org/10.1021/acsami.5b12030.

(97) Liu, C.; Yuan, J.; Masse, R.; Jia, X.; Bi, W.; Neale, Z.; Shen, T.; Xu, M.; Tian, M.; Zheng,

J.; Tian, J.; Cao, G. Interphases, Interfaces, and Surfaces of Active Materials in Rechargeable Batteries and Perovskite Solar Cells. *Adv. Mater.* **2020**, 1905245. https://doi.org/10.1002/adma.201905245.

(98) Yan, C.; Li, H. R.; Chen, X.; Zhang, X. Q.; Cheng, X. B.; Xu, R.; Huang, J. Q.; Zhang, Q. Regulating the Inner Helmholtz Plane for Stable Solid Electrolyte Interphase on Lithium Metal Anodes. *J. Am. Chem. Soc.* **2019**, *141*, 9422−9429. https://doi.org/10.1021/jacs.9b05029.

(99) De Klerk, N. J. J.; Van Der Maas, E.; Wagemaker, M. Analysis of Diffusion in Solid-State Electrolytes through MD Simulations, Improvement of the Li-Ion Conductivity in β-Li3PS4 as an Example. *ACS Appl. Energy Mater.* **2018**, *1*, 3230–3242. https://doi.org/10.1021/acsaem.8b00457.

(100) Fingerle, M.; Buchheit, R.; Sicolo, S.; Albe, K.; Hausbrand, R. Reaction and Space Charge Layer Formation at the LiCoO2-LiPON Interface: Insights on Defect Formation and Ion Energy Level Alignment by a Combined Surface Science-Simulation Approach. *Chem. Mater.* **2017**, *29*, 7675–7685. https://doi.org/10.1021/acs.chemmater.7b00890.

(101) Yang, Q.; Cui, M.; Hu, J.; Chu, F.; Zheng, Y.; Liu, J.; Li, C. Ultrathin Defective C-N Coating to Enable Nanostructured Li Plating for Li Metal Batteries. *ACS Nano* **2020**, *14*, 1866–1878. https://doi.org/10.1021/acsnano.9b08008.

(102) Jeong, S. K.; Seo, H. Y.; Kim, D. H.; Han, H. K.; Kim, J. G.; Lee, Y. B.; Iriyama, Y.; Abe, T.; Ogumi, Z. Suppression of Dendritic Lithium Formation by Using Concentrated Electrolyte Solutions. *Electrochem. commun.* **2008**, *10*, 635–638. https://doi.org/10.1016/j.elecom.2008.02.006.

(103) Yamada, Y.; Yamada, A. Review—Superconcentrated Electrolytes for Lithium Batteries. *J. Electrochem. Soc.* **2015**, *162*, A2406. https://doi.org/10.1149/2.0041514jes.

(104) Yu, L.; Chen, S.; Lee, H.; Zhang, L.; Engelhard, M. H.; Li, Q.; Jiao, S.; Liu, J.; Xu, W.; Zhang, J. G. A Localized High-Concentration Electrolyte with Optimized Solvents and Lithium Difluoro(Oxalate)Borate Additive for Stable Lithium Metal Batteries. *ACS Energy*

Lett. **2018**, *3*, 2059–2067. https://doi.org/10.1021/acsenergylett.8b00935.

(105) Suo, L.; Hu, Y. S.; Li, H.; Armand, M.; Chen, L. A New Class of Solvent-in-Salt Electrolyte for High-Energy Rechargeable Metallic Lithium Batteries. *Nat. Commun.* **2013**, *4*, 1481. https://doi.org/10.1038/ncomms2513.